Asian Journal of Water, Environment and Pollution. Vol. 22, No. 6 (2025), pp. 89-102.
doi: 10.36922/AJWEP025250204

ORIGINAL RESEARCH ARTICLE

Enhanced adsorption desulfurization performance of metal-modified Y zeolites

Jiefei Li[1]*, Xianrong Meng[1], Mingyang Song[1], and Mei Xue[2]*

[1]Department of Chemical Engineering and Technology, School of Petrochemical Engineering, Shenyang University of Technology, Liaoyang, Liaoning, China
[2]Department of Materials Physics and Chemistry, School of Chemistry and Chemical Engineering, Inner Mongolia University, Hohhot, Inner Mongolia, China
***Corresponding authors:** Jiefei Li (lijf@sut.edu.cn);
Mei Xue (setsubai@sina.cn)

Received: June 20, 2025; Revised: July 22, 2025; Accepted: July 25, 2025; Published online: August 18, 2025

Abstract: Y-zeolite is a promising adsorbent for removing organic sulfides from fuel. However, its application is limited by low adsorption capacity for refractory sulfur compounds. In this study, metal-modified Y-zeolite (MY) adsorbents, incorporating Ru^{3+}, Bi^{3+}, Zr^{4+}, and Sb^{3+} ions, were successfully synthesized via a solid-state reaction method. X-ray diffraction analysis confirmed that metal ion incorporation did not alter the crystalline framework of Y-zeolite. Nitrogen adsorption–desorption isotherms revealed that the Ru-modified Y-zeolite (RuY) possessed a notably high specific surface area of 735.23 m^2/g, whereas NH_3-temperature programmed desorption (NH_3-TPD) measurements showed that it also had the highest concentration of acidic sites (2.375 mmol/g). The effects of metal ion type, loading amount, and oxidation state on thiophene removal were systematically investigated via batch adsorption experiments. Sulfur removal efficiency increased in the following order: HY (43%) <BiY-1 (53%) <SbY-1(62%) <ZrY-1 (63%) <RuY-1 (68%). The RuY adsorbent exhibited the best adsorption performance, with Ru^{4+} ions acting as the primary active sites. The adsorption behavior followed the Langmuir isotherm model, indicating a monolayer adsorption process. Sulfur removal efficiency correlated positively with the sulfur–metal (S–M) bond strength in MY adsorbents. Compared to unmodified HY, MY adsorbents also showed improved selectivity for thiophene in the presence of competing toluene. The superior desulfurization performance of RuY is attributed to its smaller ionic radius (62 pm), higher charge (Ru^{4+}), larger specific surface area, and abundance of Lewis acid sites.

Keywords: Adsorption; Metal ion; Y-zeolite; Thiophene; Desulfurization

1. Introduction

Commercial gasoline and diesel typically contain 300–500 parts per million by weight (ppmw) of organic sulfur compounds, contributing to sulfur oxide emissions, acid rain, and particulate matter pollution.[1,2] Removing these compounds is crucial, but conventional hydrodesulphurization (HDS), though effective for sulfides, struggles to eliminate thiophene and its alkylated derivatives.[3] Ultra-low sulfur fuels (<1 ppmw) are vital for fuel cells to prevent catalyst poisoning.[4] Among various desulfurization methods, adsorption has attracted considerable attention for its ability to achieve deep desulfurization under ambient conditions.[5]

Metal ion-modified porous materials employed in the adsorption processes include zeolite, mesoporous materials, activated carbon, silica gel, alumina, mixed metal oxides, and metal organic frameworks (MOF_S).[6-13] Y-zeolite, a prototypical large-pore molecular sieve, has attracted considerable attention in adsorptive

desulfurization owing to its three-dimensional interconnected supercage structure (pore diameter ~1.3 nm) and exceptionally high specific surface area (>700 m^2/g). Its framework is enriched with abundant Brønsted and Lewis acid sites, facilitating acid-base interactions with sulfur-containing molecules and enabling efficient removal of bulky organosulfur compounds such as thiophene, benzothiophene, and dibenzothiophene. Furthermore, Y-zeolite exhibits outstanding thermal stability and highly tunable structural properties, which can be optimized through ion exchange, steam treatment, and chemical modifications.

Nevertheless, pristine Y-zeolite suffers from inherent limitations in practical applications. Its adsorption primarily relies on physical interactions and weak acid-base affinities, which are inadequate for capturing low-polarity, refractory sulfur species. Moreover, competitive adsorption of non-sulfur aromatic hydrocarbons in complex fuel matrices leads to poor selectivity, hindering the achievement of deep desulfurization at ultra-low sulfur levels (<10 ppm). In addition, repeated adsorption-regeneration cycles tend to degrade the framework's acidity and pore architecture, ultimately compromising long-term operational stability.

Incorporating metal ions into adsorbents has been shown to enhance their performance, as the introduced metal species can act as active sites for the adsorption of sulfur-containing compounds. Most studies have focused on reactive adsorption mechanisms, which can be broadly categorized into two types: (i) π-complexation-based adsorbents, such as metal-ion-exchanged Y-type zeolites (denoted as MY-zeolites, where M represents metal ions including copper(I) (Cu^+), silver(I) (Ag^+), nickel(II) (Ni^{2+}), zinc(II) (Zn^{2+}), and palladium(II) (Pd^{2+})); and (ii) adsorbents that rely on direct sulfur–metal (S–M) interactions, where the Y-type zeolite is modified with high-charge metal ions such as cerium(IV) (Ce^{4+}) and lanthanum(III) (La^{3+}).[14,15] Compared to adsorbents based on π-complexation, those utilizing direct S–M interactions generally demonstrate higher selectivity for sulfur compounds, particularly in the presence of competing aromatic hydrocarbons. Recently, new zeolite nanofiber bundle catalysts developed by Tang *et al.* demonstrated sulfur reduction to below 10 ppmw in diesel using the HDS process.[16] This has underscored the importance of adsorption selectivity over sulfur uptake in achieving the ultra-low sulfur fuel standard. A lot of high-selectivity sulfur adsorbents incorporating Ce-modified microporous materials have been reported, such as CeY,[17,18] Ce-modified mesoporous structure Y-zeolite,[19,20] Ce-doped MCM-41 frameworks,[21] aluminized MCM-41 and SBA-15 grafted with Ce^{3+},[22] Ni-Ce/alumina-silica (Al_2O_3-SiO_2),[23] Ce-Fe/activated carbon (AC) composites.[24] A few studies have also reported on the use of ruthenium complexes for the extraction of dibenzothiophene (DBT) from petroleum feedstocks. For instance, the binuclear ruthenium complex, $[CpRu(CO)_2(\mu_2\text{-}\eta^1(S)\text{: }\eta^6\text{-DBT})RuCp^*][PF_6]_2$ was used for desulfurization of DBT, in which one Ru is η^1(S)-coordinated to DBT whereas the other Ru is η^6(S)-coordinated to the same DBT molecule.[25,26] As noted, the strength of the direct S–M σ bond is mainly dependent on the metal ion's charge and ionic radius. Specific metal ions with strong ionic polarities are able to enhance direct S–M interaction and further improve adsorption selectivity for sulfur compounds.

Traditionally, the liquid phase ion-exchange method has been used to prepare the metal ion-modified Y-zeolites,[14,15,27,28] while only a few studies have explored the solid state reaction method.[29,30] In this study, the solid-state reaction method was used to develop high-selectivity S–M interaction adsorbents. A series of metal ions with high charge number and lower ionic radius—namely, ruthenium(III) (Ru^{3+}), bismuth(III) (Bi^{3+}), zirconium(IV) (Zr^{4+}), and antimony (III) (Sb^{3+})—were selected as active sites for the modification of Y-zeolite. The desulfurization performance of these MY-zeolite adsorbents was evaluated using batch adsorption of thiophene (TP) from a model gasoline containing 20 ppmw sulfur. We investigated the effect of various parameters, such as the metal type, metal ion form, chemical state, and loading amount, on the TP removal efficiency.

2. Materials and methods

2.1. Preparation of MY-zeolite (MY-1 and RuY-X series) adsorbents

Metal-ion-modified Y-type zeolite adsorbents were prepared using the solid-state ion exchange method. One gram of ammonium-exchanged Y-zeolite (NH_4Y-zeolite) was thoroughly mixed and ground for 1 h with a stoichiometric amount of ruthenium(III) chloride hydrate ($RuCl_3 \cdot xH_2O$), antimony(III) chloride ($SbCl_3$), zirconyl chloride octahydrate ($ZrOCl_2 \cdot 8H_2O$), or bismuth(III) nitrate pentahydrate ($Bi(NO_3)_3 \cdot 5H_2O$), with an initial molar ratio of metal ion to ammonium ion (M/NH_4^+) equal to 1. The mixtures were subsequently calcined in air at 500°C for 2 h. These resulting adsorbents were denoted as MY-1 and RuY-X, where M represents the metal ion (Ru^{3+}, Sb^{3+}, Zr^{4+}, or Bi^{3+}), and X indicates the initial molar ratio of ruthenium(III)

to ammonium ion. The NH_4Y-zeolite was obtained from Wako, Japan (SiO_2/Al_2O_3 = 7.0), whereas all metal salts—$RuCl_3 \cdot xH_2O$ (37.5% Ru), $ZrOCl_2 \cdot 8H_2O$ (99%), $SbCl_3$ (99%), and $Bi(NO_3)_3 \cdot 5H_2O$ (99%)—were purchased from Sinopharm Group Chemical Reagent (China). The hydrogen-form Y-zeolite (HY sample) was prepared by calcining the NH_4Y-zeolite at 500°C for 2 h in air.

2.2. Adsorption experiment

Adsorption experiments were performed using a batch method. A model gasoline solution was prepared consisting of n-heptane (99 wt%), toluene (1 wt%), and TP (20 ppmw of sulfur). N-heptane (98.5%), TP (99%), and toluene (99%) were purchased from Sinopharm Group Chemical Reagent (China). The model gasoline (10 mL) and the adsorbent (0.1 g) were mixed in a Teflon tube, and the mixture was stirred at 80°C. After adsorption, the sulfur concentration in the liquid phase was analyzed using a gas chromatograph with a flame ionization detector (GC-FID; Agilent 7890, Agilent Technologies Co., LTD., USA) equipped with a capillary column (Thermo TG-WAXMS; USA; 30 m × 0.53 mm × 1 μm).

The adsorption capacity (q_e) and sulfur removal efficiency were calculated using Equations I and II.

$$q_e = \frac{V(C_0 - C_i)}{m} \quad \text{(I)}$$

$$\text{Sulfur removal } (\%) = \frac{(C_0 - C_i)}{C_0} \times 100 \quad \text{(II)}$$

where V (mL) is the volume of model gasoline; C_0 and C_i (mg/L) are the concentrations of sulfur in the model gasoline before and after adsorption, respectively; and m (g) is the mass of adsorbents.

2.3. Adsorbent characterization

The powder X-ray diffraction (XRD) patterns were performed on a PANalytical Empyrean diffractometer (PANalytical B.V., Holland) operated at 40 kV and 40 mA, using copper K-alpha radiation. X-ray photoelectron spectroscopy (XPS) analysis was carried out using a THS-103X spectrometer (Thermo Fisher Scientific, USA) equipped with an aluminum K-alpha X-ray source (photon energy, hv = 1486.6 eV). The nitrogen (N_2) adsorption-desorption isotherms were measured on a 3H-2000PM2 system (Tianjin Xianquan Instrument Co., LTD, China) at –196°C. The adsorbents were degassed at 300°C for 5 h. The Horvath–Kawazoe (HK) method was used to calculate the surface area, based on adsorption data in the relative pressure range from 0.0000165 to 0.1546. The pore width and volume were also calculated using the HK method. Hydrogen temperature-programmed reduction (H_2-TPR) of the adsorbents was measured by a Micromeritics AutoChem 2920 analyzer (Micromeritics Instrument Co., LTD, USA). The adsorbents were swiped at 300°C for 30 min under helium flow (10 mL/min) and then cooled to 40°C before being reacted with H_2. The profile was recorded by increasing the temperature from 100°C to 800°C at a ramp rate of 10°C/min.

Temperature-programmed desorption of ammonia (NH_3-TPD) was used to calculate the intensity and number of acidic sites in the adsorbents. This was conducted using a TP-5080 automatic analyzer (Tianjin Xianquan Instrument Co., LTD, China). About 0.1 g of adsorbent was placed in a U-shaped quartz microreactor. The adsorbent was activated at 550°C for 30 min under helium flow (20 mL/min), cooled to 100°C, then exposed to ammonia. The adsorbents were flushed again in helium for 3 h to remove any physisorbed ammonia. A desorption profile was then recorded by increasing the adsorbent temperature from 100°C to 800°C at a ramp rate of 10°C/min.

The pyridine-Fourier transform infrared (Py-FTIR) was used to analyze the amount and type of acidic sites, with pyridine as the probe molecule. Measurements were conducted using an FTIR spectrometer (Tensor 27, BRUKER Technology Co., LTD, USA). Transmission electron microscopy (TEM) imaging was performed on a FEI Tecnai F20 system (FEI Co., LTD, USA) operated at an accelerating voltage of 200 kV. The size and morphology of the adsorbents were observed by using field emission scanning electron microscopy (FE-SEM) (Hitachi s-4800, Hitachi, Japan).

3. Results and discussion

3.1. Adsorbent characterization

3.1.1 XRD analysis of adsorbents

XRD patterns of the MY-1 adsorbents and NH_4Y-zeolite are shown in Figure 1. Both adsorbents maintained the characteristic framework structure of NH_4Y-zeolite framework, although a reduction in the intensity of some diffraction peaks was observed for the MY-1 samples. This decrease is attributed to partial lattice collapse following calcination treatment. In addition to the typical diffraction peaks of NH_4Y-zeolite, the BiY-1, ZrY-1, and RuY-1 samples exhibited the additional peaks corresponding to the oxide phases of the incorporated metals. Specifically, diffraction peaks for

Bi_2O_3 at the (012) plane (JCPDF No.: 41-1449), ZrO_2 at the (111) plane (JCPDF No.: 37-1484), and RuO_2 at the (101) and (110) planes (JCPDF No.: 43-1027) were observed. Interestingly, SbY-1 did not show detectable diffraction peaks corresponding to Sb oxide. However, energy-dispersive X-ray spectroscopy (EDX) analysis (Figure S1B) confirmed the presence of Sb elements, suggesting a high degree of homogeneity and dispersion of Sb within the Y-zeolite matrix.

These results indicate that, except for SbY-1, the MY-1 adsorbents consist of two distinct phases: a MY-zeolite phase and a bulk metal oxide phase (M_xO_y). In contrast, SbY-1 appears to be a single-phase system with Sb ions uniformly dispersed within the zeolite.

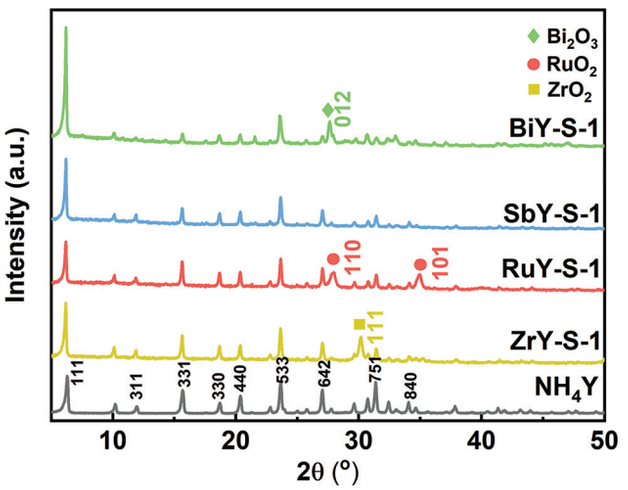

Figure 1. XRD patterns of NH_4Y and MY-1 adsorbents. The characteristic peaks of the metal oxides are marked.

Abbreviations: Bi_2O_3: Bismuth(III) oxide; MY: Metal ion-modified Y-zeolite; NH_4Y: Ammonium-form Y-zeolite; RuO_2: Ruthenium(IV) oxide; SbY: Antimony-modified Y-zeolite; XRD: X-ray diffraction; Y-zeolite: Faujasite-type zeolite; ZrO_2: Zirconium(IV) oxide.

The XRD patterns of the Ru-modified zeolites with varying initial molar ratios of Ru to ammonium ion (Ru/NH_4^+) are shown in Figure S2. All samples exhibited characteristic peaks of Y-zeolite along with the RuO_2 phase. As the Ru/NH_4^+ ratio decreased, the intensity of the RuO_2 diffraction peaks also diminished, indicating reduced loading of bulk RuO_2 with lower initial Ru content.

3.1.2. SEM and TEM images of adsorbents

The SEM (Figure 2) image exhibited that MY-1 adsorbents retained the particle morphology of the original NH_4Y, exhibiting particles with crystal habits smaller than 0.9 μm.

The morphology and elemental distribution of MY-1 were further examined using SEM and EDX. The SEM image exhibited that MY-1 adsorbents retained the particle morphology of the original NH_4Y, exhibiting particles with crystal habits smaller than 0.9 μm. The SEM images of RuY-1 and ZrY-1 showed that Y-zeolite particles were covered by bulk RuO_2 and ZrO_2 nanoparticles, respectively. In contrast, the BiY-1 sample exhibited particle conglutination. The EDX (Figure S1) spectra confirmed the presence of Ru, Sb, Bi, and Zr in their respective MY-1 samples. The metal content of RuY-1, SbY-1, ZrY-1 and BiY-1 was 5.02, 13.85, 10.28 and 16.22 wt%, respectively (Table S1).

Low magnification TEM images of NH_4Y-zeolite and the RuY-X series are shown in Figure 3. The nano-rod-like particles of RuO_2 with a width of 30–40 nm and a length of 30–100 nm can be observed at the surfaces of RuY-1 and RuY-1/2 samples. In contrast, RuO_2 was not observed in RuY-1/4, RuY-1/8, and RuY-1/16 samples, indicating a significant reduction in RuO_2 content with decreasing initial Ru (Ru/NH_4^+ mole ratio from 1 to 1/16). These observations are consistent with the XRD results (Figure S1). The high-resolution TEM image of RuO_2 is shown in the inset of Figure 3B,

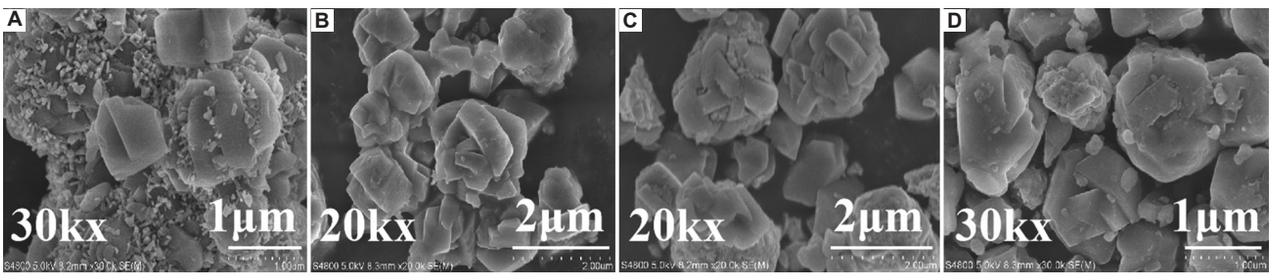

Figure 2. SEM images of adsorbents. (A) RuY-1. (B) SbY-1. (C) BiY-1. (D) ZrY-1.

Abbreviations: BiY: Bismuth-modified Y-zeolite; RuY: Ruthenium-modified Y-zeolite; SbY: Antimony-modified Y-zeolite; SEM: Scanning electron microscopy; ZrY: Zirconium-modified Y-zeolite.

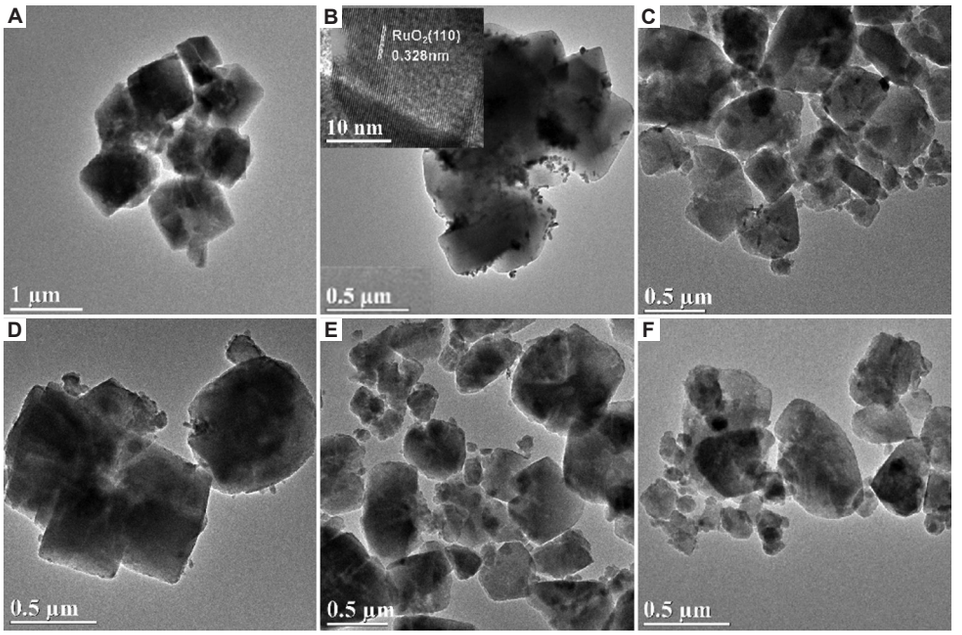

Figure 3. TEM image of adsorbents. (A) NH_4Y. (B) RuY-1. (C) RuY-1/2. (D) RuY-1/4. (E) RuY-1/8. (F) RuY-1/16. Abbreviations: NH4Y: Ammonium-form Y-zeolite; RuY: Ruthenium-modified Y-zeolite; TEM: Transmission electron microscopy.

where a lattice fringe of 0.328 nm corresponds to the (110) plane of single-crystalline RuO_2. Based on combined XRD, SEM, and TEM studies, we propose the following mechanism for MY-1 formation during calcination: a portion of the NH_4^+ ions in NH_4Y-zeolite undergo thermal decomposition to volatilize NH_3, whereas another portion is ion-exchanged with the added metal ions, which diffuse into the Y-zeolite framework to form MY. The residual metal salts that are not incorporated into the framework are converted into bulk metal oxide phases (M_xO_y). Therefore, MY-1 adsorbent is not a simple MY zeolite phase, which consists of MY zeolite and bulk M_xO_y phases.

3.1.3. XPS results of adsorbents

The chemical state of metal species in the MY-1 sample was investigated by XPS study. Figure 4 presents the Ru 3d spectrum of the RuY-1 sample, with $RuCl_3 \cdot xH_2O$ used as the reference for Ru^{3+}. The C 1s peak at 284.8 eV likely originates from carbonaceous contamination.[31,32] Due to the overlap between the C 1s and Ru $3d_{3/2}$, only the Ru $3d_{5/2}$ binding energy region is discussed. In the $RuCl_3 \cdot xH_2O$ sample, the peak at a binding energy of 281.5 eV corresponds to Ru^{3+}. In the RuY-1 sample, the Ru $3d_{5/2}$ peak appears at 281.2 eV, which is assigned to Ru^{4+}. This peak is slightly shifted to a higher binding energy compared to that of bulk RuO_2 (280.7 eV). The Ru^{4+} species in RuY-1 may exist in the form of RuO_x cluster ions, such as $Ru(IV)O_x^{(4-2x)+}$ ($0 < x < 2$). Several studies have reported that Ru cluster ions are more electron-deficient than bulk RuO_2.[33-35]

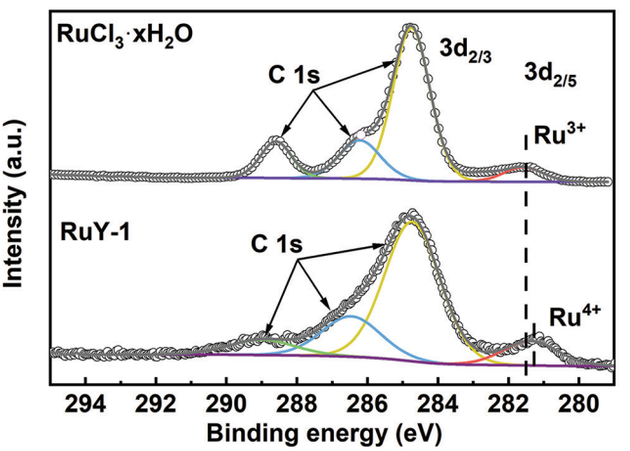

Figure 4. XPS spectra of the RuY-1 adsorbent. Abbreviations: RuY: Ruthenium-modified Y-zeolite; XPS: X-ray photoelectron spectroscopy.

XPS spectra of the SbY-1, ZrY-1, and BiY-1 samples are displayed in Figure S3, with $SbCl_3$, $ZrOCl_2 \cdot 8H_2O$, and $Bi(NO_3)_3 \cdot 5H_2O$ used as references for Sb^{3+}, Zr^{4+} and Bi^{3+}, respectively. Three characteristic peaks are observed in the Sb 3d spectrum of SbY-1: two peaks at 530.7eV ($3d_{5/2}$) and 540.1eV ($3d_{3/2}$) corresponding to Sb^{3+} of $SbCl_3$ and Sb_2O_3, and another peak at

532.1eV corresponding to Sb^{5+} of Sb_2O_5, indicating the coexistence of Sb^{3+} and Sb^{5+} in the SbY-1 sample.[36] The peak area of Sb^{5+} is smaller than that of Sb^{3+}, indicating that the Sb(III)Y in the SbY-1 is the dominant phase.

In the Zr 3d spectrum, peaks at 182.5 eV ($3d_{5/2}$) and 185 eV ($3d_{3/2}$) are attributed to Zr^{4+} for the $ZrOCl_2 \cdot 8H_2O$ and bulk ZrO_2.[37] The peaks at 182.7 eV ($3d_{5/2}$) and 185.2eV($3d_{3/2}$) for the ZrY-1 are shifted slightly by 0.2eV toward higher binding energy, and are attributed to Zr^{4+}. Similar to RuY-1, the Zr^{4+} species may exist as ZrO_x cluster ions in ZrY-1. In the Bi 4f spectrum of BiY-1, the peaks at 159.8 eV ($4f_{7/2}$) and 165.2 eV ($4f_{5/2}$) are attributed to Bi^{3+}, consistent with $Bi(NO_3)_3 \cdot 5H_2O$ and BiOCl references.[38]

These findings indicate oxidation of the metal species occurred in the RuY-1and SbY-1 samples during the calcinations at 500°C, but not in the ZrY-1 and BiY-1 samples. The chemical state of metal species in RuY-1and SbY-1 adsorbents was changed to Ru^{4+} and Sb^{5+}. This suggests that metal species in MY-zeolite do not exist as simple metal ions (M^{n+}), but rather as MOx cluster ions. For example, in RuY, the Ru species likely exist in a cluster form. It is well known that tetravalent metal ions usually exist as polymeric or cluster oxide or hydroxide ions.[34]

To further investigate the distribution of Ru species in Y-zeolite micropores, depth-profile XPS analysis of the RuY-1/2 sample was conducted at different penetration depths (10, 20, and 30 nm). The XPS spectra are shown in Figure S4. The Ru $3d_{5/2}$ peak at 281.2eV at all penetration depths confirms the presence of Ru^{4+} species within the Y-zeolite micropores.

3.1.4. H_2-TPR of adsorbents

H_2-TPR is often used to investigate the metal-support interaction and surface properties such as metal stability, species, and distribution. To gain deep insight into the location of Ru species in the RuY-X samples, the reducibility of RuY-X and NH_4Y-zeolite samples was studied using H_2-TPR (Figure 5). No reduction peak was observed for the NH_4Y-zeolite, indicating that it does not consume hydrogen in this temperature range. RuY-1 showed several reduction peaks, indicating the existence of different kinds of Ru oxide species. The peak at 133°C corresponds to the reduction of supported RuO_2 nanoparticles on the external surface of Y-zeolite, whereas the peak located at 163°C corresponds to the reduction of RuOx clusters in the supercages of the Y-zeolite, where they strongly interact with the framework.[33] The peak centered at 300–550°C is attributed to RuOx clusters located in the small inner channels of Y-zeolite, such as the sodalite unit or hexagonal prism. These clusters exhibit stronger interactions with the framework, making them more resistant to hydrogen reduction. These results suggest that calcination of RuY-1 led to partial migration of Ru species from supercages into the smaller internal channels. Similar reduction patterns were observed in RuY-1/2 and RuY-1/8 samples. However, the RuY-1/8 sample lacked the reduction peak corresponding to RuO_x clusters in the supercages. Literature reports indicate that the reducibility of metal species in zeolites typically follows the order: supercage >sodalite cage >hexagonal prism.[39-41] Based on TEM, XPS, and H_2-TPR results, it can be concluded that Ru species in RuY-X samples are primarily present as RuO_2 nanoparticles on the external surface and as RuO_x clusters dispersed within both supercages and inner channels of the Y-zeolite.

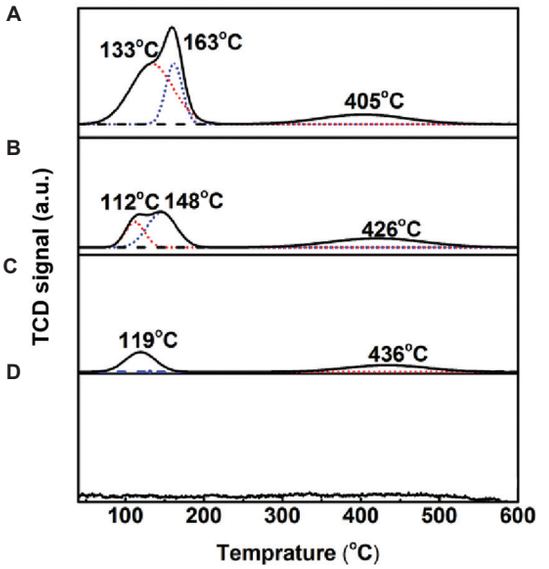

Figure 5. H_2-TPR spectra of adsorbents. (A) NH_4Y. (B) RuY-1/8. (C) RuY-1/2. (D) RuY-1.
Abbreviations: H_2-TPR: Hydrogen temperature-programmed reduction; NH_4Y: Ammonium-form Y-zeolite; RuY: Ruthenium-modified Y-zeolite; TCD: Thermal conductivity detector; TEM: Transmission electron microscopy.

3.1.5. Py-FTIR spectra of adsorbents

To investigate the effects of acidity present in the MY-1 adsorbents on the TP removal performance, the acidity of MY-1 was determined by Py-FTIR analysis (Figure 6). Since pyridine molecules are too large to enter the micropore channel of Y-zeolite, Py-FTIR analysis only detects acidity on the external surface.

Two types of acid sites were identified on the external surface of MY-1: one peak at 1540 cm^{-1} corresponding to the vibration of pyridine molecules bound at Brønsted acid sites and the other peak at 1450 cm^{-1} attributed to the ring C-C stretching vibration of pyridine adsorbed on Lewis acid sites. Another intense band was observed at 1490 cm^{-1}, arising from the combined presence of Lewis acidic and Brønsted acid sites.[42,43] These results indicate that MY-1 adsorbents possess both Lewis acidic and Brønsted acid sites, suggesting that the incorporation of metal ions modifies the acidity of the adsorbent surfaces.

Quantitative data on acid site concentrations are presented in Table 1. The total acidity (T) and strong acidity (S) were calculated by desorption of pyridine at 150°C and 450°C, respectively. The difference between T and S corresponds to the content of weak acid sites (W). The concentrations of Lewis acid and Brønsted acid sites were calculated using Equations III and IV.

$$L\ (mol/g) = 3.73 \times A_L \quad (III)$$

$$B\ (mol/g) = 9.90 \times A_B \quad (IV)$$

where L and B are the concentrations of Lewis acid and Brønsted acid (mol/g), respectively, and A_L and A_B are the absorbance intensity at 1450 cm^{-1} and 1540 cm^{-1}, respectively.[44]

The T of the MY-1 external surface follows the order: SbY-1 >ZrY-1 >BiY-1 >RuY-1. For all samples, the Brønsted acid site concentration (T_B) was greater than that of Lewis acid sites (T_L). SbY-1 exhibited the strongest acidity, consistent with the XRD analysis, which identified SbY as its main crystalline phase. These findings suggest that the acidity of MY-1's external surface is mainly contributed by the metal ions within the MY structure, whereas the M_xO_y contributes minimally. RuY-1 sample exhibited the weakest acidity, with barely visible peaks in the magnified view of Figure S5. Notably, it had the lowest Lewis acidity (S_L = 0.38 × 10^{-4} mol/g), suggesting a limited presence of Ru ions on the external surface of RuY-1.[19,45]

3.1.6. NH_3-TPD of adsorbents

Pyridine-FTIR can only detect the external surface acidity of MY-1 samples. However, the NH_3 molecule is smaller than the pyridine molecule and can easily enter

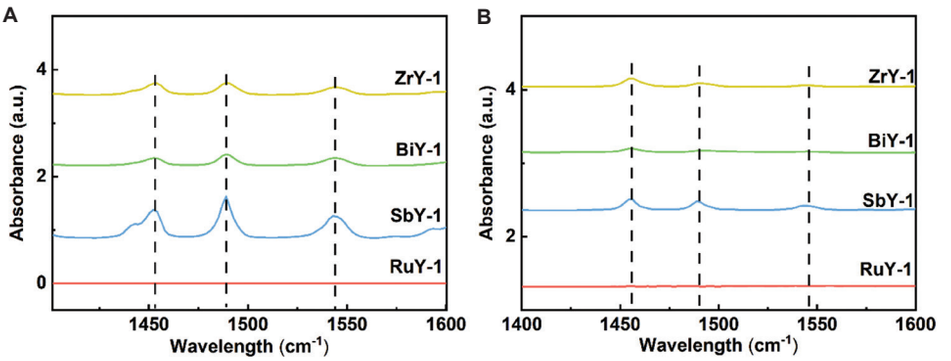

Figure 6. Py-FTIR pattern of MY-1 adsorbents. Spectrum after desorption of pyridine at 150 °C (A) and 450°C (B) are shown.

Abbreviations: BiY: Bismuth-modified Y-zeolite; PY-FTIR: Pyridine-Fourier-transform infrared spectroscopy; RuY: Ruthenium-modified Y-zeolite; SbY: Antimony-modified Y-zeolite; ZrY: Zirconium-modified Y-zeolite.

Table 1. Surface acid content of MY-1 adsorbents

Adsorbents	Concentration (10^{-4} mol/g)						
	T	T_B	T_L	S_B	S_L	W_B	W_L
SbY-1	56.16	38.13	18.03	9.50	4.05	28.63	13.98
ZrY-1	22.4	14.15	8.09	1.06	3.96	13.09	4.13
BiY-1	18.9	13.73	5.17	0.76	1.81	12.97	3.36
RuY-1	1.28	0.82	0.46	0	0.38	0.82	0.08

Abbreviations: MY: Metal ion-modified Y-zeolite; T: Total acid; T_B: Total Brønsted acid; T_L: Total Lewis acid; S_B: Strong Brønsted acid; S_L: Strong Lewis acid; W_B: Weak Brønsted acid; W_L: Weak Lewis acid.

the micropore channels of Y-zeolite. Therefore, the acidity of MY-1 was further investigated using NH_3-TPD analysis. The NH_3-TPD spectra of the MY-1 adsorbents are shown in Figure 7. The total acidic content of MY-1 decreased in the following order: RuY-1 (2.375 mmol/g) >HY (1.821 mmol/g) >SbY-1 (1.344 mmol/g) >ZrY-1 (1.205 mmol/g) >BiY-1 (1.196 mmol/g). The SbY-1, ZrY-1, and BiY-1 samples displayed similar NH_3 desorption peak intensities in the temperature range of 100–500°C. A desorption peak around 190°C corresponds to physisorbed NH_3, whereas the peak near 300°C indicates the presence of weak acidic sites. The peak at approximately 420°C is assigned to strong acidic sites, likely contributed by the metal species incorporated into the MY-1 samples. RuY-1 exhibited a broad and asymmetric NH_3 desorption peak over a wide temperature range (100–800°C), suggesting the presence of multiple types of acid sites associated with Ru cluster ions. Specifically, desorption peaks at 400°C and 640°C were attributed to strong acidic sites. According to previous studies, NH_3-TPD analysis of ZSM-type zeolite shows desorption peaks at 60–100°C (physisorbed NH_3 on the external surface), 150–230°C (weak acidic sites), and 420–500°C (strong acidic sites), with the latter attributed to a mixture of Brønsted and Lewis acid sites.[46]

From these acidity studies, we propose that the concentration of Ru cluster ions on the external surface of RuY-1 zeolite is relatively low. This conclusion is supported by Py-FTIR results, which revealed weak acid intensity and the lowest Lewis acidity for RuY-1. However, the NH_3-TPD results indicate that most of the Ru cluster ions are located within the micropores of Y-zeolite, contributing significantly to strong acidity at high temperatures. These internal Ru cluster ions are expected to play an important role in the desulfurization of TP. Nickel (Ni)-supported mesoporous AlMCM-41 and Ni-modified mesoporous silica have also been reported for the desulfurization of fuel. Ni enhances both Brønsted and Lewis acid site intensity, and such high acidity will play a significant role in fuel desulfurization.[21,47]

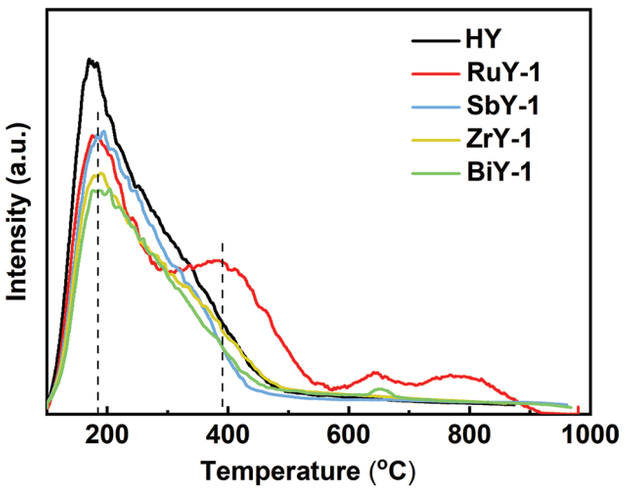

Figure 7. NH_3-TPD profiles of the adsorbents. Abbreviations: BiY: Bismuth-modified Y-zeolite; HY: Proton-form Y-zeolite; NH_3: Ammonia; RuY: Ruthenium-modified Y-zeolite; SbY: Antimony-modified Y-zeolite; TPD: Temperature-programmed desorption; ZrY: Zirconium-modified Y-zeolite.

3.1.7. N_2 adsorption-desorption isotherms of adsorbents

Figure 8 and Table S2 display the N_2 adsorption-desorption isotherms and pore structure parameters of the MY-1 and NH_4Y samples. Adsorption isotherms correspond to Brunauer–Deming–Deming–Teller type I isotherms with a single pore size distribution. Brunauer–Emmett–Teller (BET) surface area decreases in the order: NH_4Y-zeolite >RuY-1 >ZrY-1 >SbY-1 >BiY-1. This decline is likely due to the partial blockage of the microporous channels in Y zeolite and/or the conglutination of zeolite particles. A reduction in BET surface area mass transfer efficiency interrupts interaction between the internal active sites and the adsorbed molecules.[48] BiY-1 showed the smallest external area (28.16 m^2/g), indicating that significant agglomeration of Y-zeolite particles after calcination treatment, which is in agreement with the SEM images (Figure 2C). The internal surface area and total pore volume also decreased in the order: NH_4Y-zeolite >RuY-1 >ZrY-1 >SbY-1 >BiY-1, suggesting that more M^{n+} entered the Y-zeolite micropore.[49]

3.2. Selective adsorption of TP

3.2.1. Effect of metal species on TP adsorption

The TP adsorption from model gasoline (containing toluene) was studied using batch adsorption experiments over various MY-1 and HY. The S removal increases in the following order: HY (16%) <BiY-1 (20%) <ZrY-1 (25%) <SbY-1(27%) <RuY-1 (38%) (Figure 9). MY-1 samples showed higher sulfur removal compared to the HY sample, suggesting that the metal species in the Y-zeolite play an important role in the selective adsorption of TP. Song *et al.*[45] also reported that HY has a large number of Brønsted acid sites, which are harmful to the desulfurization process.

RuY-1 showed the best sulfur removal performance among all samples. Structural characterization using the

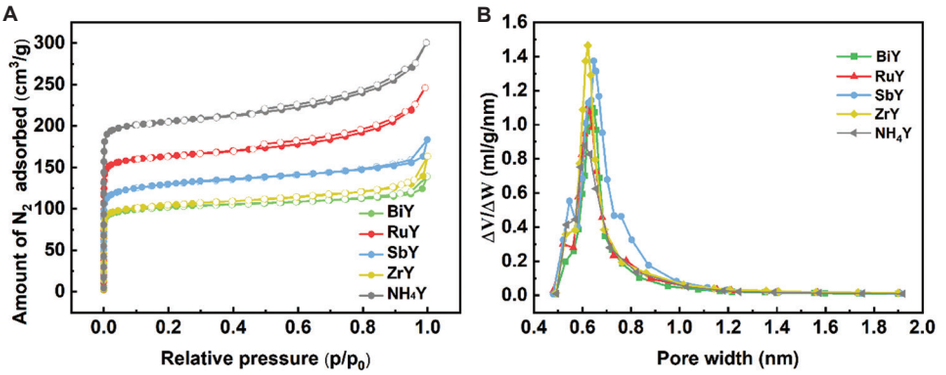

Figure 8. Characteristics of adsorption isotherms of NH_4Y and MY-1 adsorbents. (A) N_2 adsorption-desorption isotherms. (B) Pore size distribution.

Abbreviations: BiY: Bismuth-modified Y-zeolite; MY: Metal ion-modified Y-zeolite; NH4Y: Ammonium-form Y-zeolite; p: Gas pressure at adsorption equilibrium; P_0: Saturation vapor pressure of nitrogen at the experimental temperature; RuY: Ruthenium-modified Y-zeolite; SbY: Antimony-modified Y-zeolite; V: Volume of adsorbed nitrogen under standard temperature and pressure (STP) conditions; W: Weight of the adsorbate (nitrogen); ZrY: Zirconium-modified Y-zeolite.

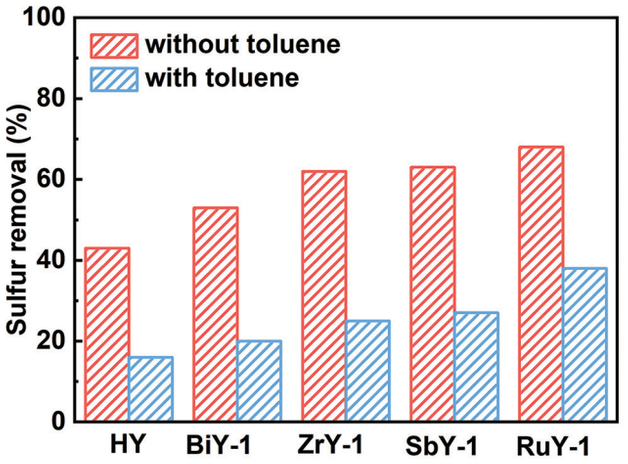

Figure 9. Sulfur removal performance of MY-1 and HY adsorbents from model gasoline with or without toluene. Adsorption conditions: initial sulfur concentration = 20 ppm; model gasoline volume: 10 mL; adsorbent weight = 0.1 g, temperature = 80°C; contact time = 2 h.

Abbreviations: BiY: Bismuth-modified Y-zeolite; HY: Proton-form Y-zeolite; MY: Metal ion-modified Y-zeolite; RuY: Ruthenium-modified Y-zeolite; SbY: Antimony-modified Y-zeolite; ZrY: Zirconium-modified Y-zeolite.

XRD and TEM study indicated that the RuY-1 sample contains both Ru-incorporated Y-zeolite and bulk RuO_2 phases. To clarify the TP adsorptive properties of bulk RuO_2, the simple bulk RuO_2 phase was prepared by calcination of $RuCl_3 \cdot xH_2O$ in air at 500°C. The sample showed a 16% lower sulfur removal, confirming that the M_xO_y phase generally shows poor TP adsorptive properties.[5] Therefore, the MY component of MY-1, rather than the MxOy, plays an important role in TP selectivity. Interestingly, SbY-1 showed high TP selectivity, possibly due to the lower loading or weaker clustering of SbxOy species within the Y-zeolite compared to RuOx. This suggests that sulfur removal efficiency is not only dependent on the M^{n+} type but also on its loading amount.

Commercial gasoline contains TP derivatives, olefins, and aromatic compounds.[18] To investigate the influence of toluene as a competing adsorbate, the TP experiments adsorption was carried out using a model gasoline without toluene (Figure 9). The sulfur removal improved in the following order: HY (43%) <BiY-1 (53%) <SbY-1(62%) <ZrY-1 (63%) <RuY-1 (68%). The desulfurization performance of RuY-1 is comparable to that of other adsorbents reported in Table S3. These results indicate competitive adsorption between toluene and TP, and further confirm the superior selectivity of RuY-1 for sulfur compounds.

3.2.2. Effect of Ru loading of RuY-X for TP adsorption

Since RuY-1 showed high selectivity for TP, a more detailed study was carried out to assess the effect of Ru loading of RuY-X on TP removal (Figure 10). The sulfur removal improved in the following order: RuY-1/2(N_2) (3%) <RuY-1/16 (23%) <RuY-1/8 (28%) <RuY-1/4 (36%) <RuY-1(38%) <RuY-1/2 (44%). RuY-1/2 showed maximum sulfur removal, and this

performance improved with increasing Ru/NH_4^+ molar ratio, suggesting that sulfur removal is strongly dependent on the RuOx clusters present in the RuY-X sample. However, further increases in Ru loading beyond this ratio slightly reduced sulfur removal, likely due to the formation of bulk RuO_2 nanocrystals, which may block the micropores of the Y-zeolite. The RuY-1/2(N_2) sample containing Ru3+ species showed a sulfur removal of only 3%, much lower than that of RuY-1/2 (44%), indicating that Ru^{4+} is more effective for thiophene adsorption.

3.2.3. Effects of adsorbent acidity on TP adsorption

NH_3-TPD analysis showed that the RuY-1 sample exhibits the highest concentration of strong acid sites among the MY-1 series, despite showing the lowest Lewis acidity on the external surface area as observed in the Py-IR study. Meanwhile, the BET study showed that the RuY-1 sample had the largest internal surface area of 665 m^2/g. Based on these findings, it is proposed that the acidity of RuY-1 is predominantly contributed by RuOx clusters located within the internal surface area (micropores) of the Y-zeolite. These RuOx clusters, particularly those containing Ru^{4+}, serve as active sites and significantly enhance thiophene removal.

The distribution of RuOx clusters in the RuY-X series was further studied using H_2-TPR. The results confirmed that the RuOx clusters are highly dispersed within both the supercages and the internal channels of the Y-zeolite. However, only the RuOx clusters located in the supercages contribute significantly to TP selectivity, whereas those migrating into the inner channels show negligible adsorption capability[18]. Furthermore, the H_2-TPR reduction peak area correlates with the amount of RuOx clusters, and RuY-1/2 showed a slightly higher reduction peak area than RuY-1.

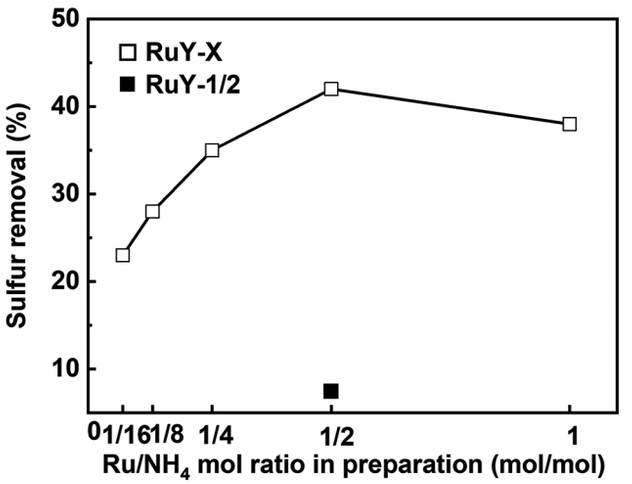

Figure 10. Effect of Ru loading amount in RuY-X on sulfur removal. Adsorption conditions: initial sulfur concentration = 20 ppm; model gasoline volume = 10 mL; adsorbent weight = 0.1 g; temperature = 80°C; contact time = 2 h.

Abbreviations: Ru: Ruthenium; RuY: Ruthenium-modified Y-zeolite.

3.3. Adsorption isotherm

The adsorption isotherms were investigated through batch adsorption experiments. Two models were used to describe the equilibrium data: (1) The Langmuir model explains properties such as physisorption with homogeneous monolayer adsorption, in which all the active sites are equivalent and independent; (2) The Freundlich model is an empirical model that describes adsorption on heterogeneous surfaces and multilayer adsorption. The Langmuir equation and the Freundlich equation are described in Equations V and VI, respectively.[50,51]

$$\frac{C_e}{q_e} = \frac{1}{q_m K_L} + \frac{C_e}{q_m} \quad \text{(V)}$$

$$q_e = K_F C_e^{1/n} \quad \text{(VI)}$$

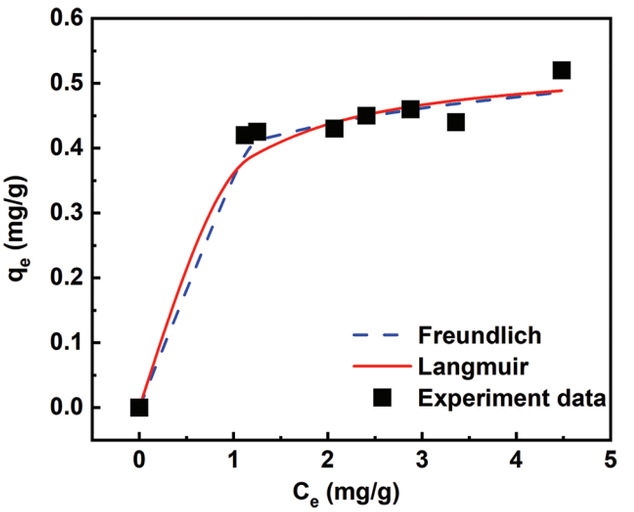

Figure 11. Adsorption isotherm for TP using RuY-1/2 adsorbent. Experimental conditions: Initial TP concentration = 20 ppm; model gasoline volume = 10 mL; adsorbent weight = 0.1 g; temperature = 80°C; contact time = 2 h.

Abbreviations: C_e: Remaining concentration of TP at equilibrium (mg/L), q_e: Amount of TP adsorbed at equilibrium (mg/g); RuY: Ruthenium-modified Y-zeolite; TP: Thiophene.

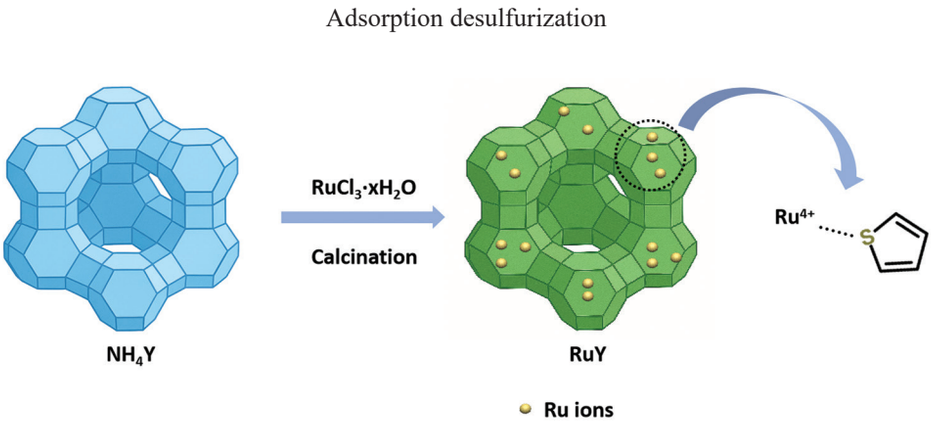

Figure 12. The adsorption mechanism diagram of TP on the RuY adsorbent.
Abbreviations: NH_4Y: Ammonium-form Y-zeolite; Ru: Ruthenium; RuY: Ruthenium-modified Y-zeolite.

Table 2. Langmuir and Freundlich isotherm parameters for TP adsorption on RuY-1/2 adsorbent

Model	K_L	q_m (mg/g)	n	K_F	R^2
Langmuir	1.52	0.488	-	-	0.975
Freundlich	-	-	7.704	0.412	0.687

Abbreviations: K_F: Freundlich constant; K_L: Langmuir constant; n: Freundlich heterogeneity factor; q_m: Maximum adsorption capacity; R^2: Coefficient of determination; TP: Thiophene.

where C_e is the remaining concentration of TP at equilibrium (mg/L), q_e is the amount of TP adsorbed at equilibrium (mg/g), q_m is the theoretical maximum adsorption capacity (mg/g), K_L is the Langmuir isotherm constant (L/mg) reflecting the strength of adsorption, K_F is the Freundlich isotherm constant (L/mg) related to multilayer adsorption capacity, and n is the Freundlich empirical constant related to the intensity of adsorption.

The adsorption isotherm of TP on RuY-1/2 adsorbent at 80°C is shown in Figure 11. The equilibrium parameters of the model are summarized in Table 2. The calculated n is 7.074, and 1/n ranges from 0.1 to 0.5, suggesting that the adsorption process can easily occur. The adsorption data fit the Langmuir model better than the Freundlich model, with a higher correlation coefficient (R^2 = 0.9758) compared to the Freundlich model (R^2 = 0.6873). This indicates that TP adsorption on RuY-1/2 proceeds primarily via monolayer adsorption onto a homogeneous surface.

Based on the direct S–M interaction mechanism for thiophene adsorption, the σ-bond interaction between sulfur and metal cations (e.g., Ce^{4+} in CeY, La^{3+} in LaY) is stronger than the π-complexation interaction (e.g., Cu^+ in CuY, Ag^+ in AgY), offering better selectivity and efficiency for ultra-deep desulfurization.[14,29] The S–M σ bond strength depends on the valence state and ionic radius of the M^{n+} in the MY adsorbents. XPS analysis confirmed the oxidation states of the metal ions in the MY-1 adsorbents as Bi^{3+}, Sb^{3+}, Sb^{5+}, Ru^{4+}, and Zr^{4+}. Their ionic radii are as follows: Bi^{3+}: 103 pm; Zr^{4+}: 72 pm; Ru^{3+}: 68 pm; Ru^{4+}: 62 pm; and Sb^{5+}: 60 pm. Smaller ionic radius and higher charge enhance polarization energy, leading to stronger S–M bond formation. Among the tested adsorbents, RuY-1 showed the highest sulfur removal, confirming that Ru^{4+} forms stronger S–M σ bonds than Zr^{4+} or Bi^{3+}. This suggests that smaller-radius and higher-valent metal ions promote stronger interactions with thiophene molecules, enhancing selective adsorption (Figure 12).

4. Conclusion

Metal ion modified MY-1 zeolite adsorbents exhibit selective adsorption for TP from low-sulfur concentration model gasoline. The solid-state reaction method proves effective for preparing these MY-1 adsorbents. Among them, the RuY-1/2 adsorbent, modified with Ru^{4+} cluster ion, showed the highest sulfur removal efficiency. The selectivity of MY-type adsorbents for TP depends on key properties of the incorporated metal ions: smaller ionic radius, higher charge, and greater concentration of Lewis acid sites.

Acknowledgments

None.

Funding

This study was supported by the Basic Scientific Research Project of the Higher Education Department of Liaoning Province (LJ212410142153), Liaoning Province Science and Technology Plan Joint Plan

(Fund) Project (2023-BSBA-251), and Natural Science Foundation of China (No. 21266014).

Conflict of interest

The authors declare no competing interests.

Author contributions

Conceptualization: Mei Xue
Formal analysis: Mingyang Song
Investigation: Xianrong Meng
Methodology: Xianrong Meng
Writing–original draft: Jiefei Li
Writing–review & editing: Mei Xue

Availability of data

Data are available from the corresponding author upon reasonable request

References

1. Yang RT, Hernández-Maldonado AJ, Yang FH. Desulfurization of transportation fuels with zeolites under ambient conditions. *Sci Rep.* 2003;301:79-81. doi: 10.1126/science.1085313
2. Xiao J, Wang X, Fujii M, Yang Q, Chen Y, Song C. A novel approach for ultra-deep adsorptive desulfurization of diesel fuel over TiO_2-CeO_2/MCM-48 under ambient conditions. *AIChE J.* 2013;59:1441-1445. doi: 10.1002/aic.14045
3. Jeevanandam P, Klabunde KJ, Tetzler SH. Adsorption of thiophenes out of hydrocarbons using metal-impregnated nanocrystalline aluminum oxide. *Microporous Mesoporous Mater.* 2005;79:101-110. doi: 10.1016/j.micromeso.2004.09.005
4. Hernández-Maldonado AJ, Yang RT. Denitrogenation of transportation fuels by zeolites at ambient temperature and pressure. *Angew Chem Int Ed.* 2004;116:1022-1022. doi: 10.1002/ange.200462998
5. Xue M, Wen P, Chitrakar R, Ooi K, Feng Q. Screening of inorganic adsorbents for selective adsorption of thiophene from model gasoline. *Sep Sci Technol.* 2012;47:1926-1936. doi: 10.1080/01496395.2012.663755
6. Xue M, Chitrakar R, Sakane K, *et al*. Selective adsorption of thiophene and 1-benzothiophene on metal-ion-exchanged zeolites in organic medium. *J Colloid Interface Sci.* 2005;285:487-492. doi: 10.1016/j.jcis.2004.12.031
7. Tan P, Qin J, Liu X, Yin X, Sun L. Fabrication of magnetically responsive core-shell adsorbents for thiophene capture: $AgNO_3$-functionalized Fe_3O_4@ mesoporous SiO_2 microspheres. *J Mater Chem A.* 2014;2:4698-4705. doi: 10.1039/c3ta15026b
8. Saleh TA, Sulaiman KO, AL-Hammadi SA, Dafalla H, Danmaliki GI. Adsorptive desulfurization of thiophene, benzothiophene and dibenzothiophene over activated carbon manganese oxide nanocomposite: With column system evaluation. *J Clean Prod.* 2017;154:401-412. doi: 10.1016/j.jclepro.2017.04.008
9. Subhan F, Liu BS. Acidic sites and deep desulfurization performance of nickel supported mesoporous AlMCM-41 sorbents. *Chem Eng J.* 2011;178:69-77. doi: 10.1016/j.cej.2011.10.024
10. Xiao J, Sitamraju S, Chen Y, *et al*. Air-promoted adsorptive desulfurization of diesel fuel over Ti-Ce mixed metal oxides. *AIChE J.* 2015;61:631-639. doi: 10.1002/aic.14617
11. Chang G, Huang M, Su Y, *et al*. Immobilization of Ag(I) into a metal-organic framework with -SO_3H sites for highly selective olefin-paraffin separation at room temperature. *Chem Commun.* 2015;51:2859-2862. doi: 10.1039/C4CC09008B
12. Ahmad K, Nazir MA, Qureshi AK, *et al*. Engineering of zirconium based metal-organic frameworks (Zr-MOFs) as efficient adsorbents. *Mater Sci Eng B.* 2020;262:114766. doi: 10.1016/j.mseb.2020.114766
13. Khan NA, Najam T, Shah SSA, *et al*. Development of Mn-PBA on GO sheets for adsorptive removal of ciprofloxacin from water: Kinetics, isothermal, thermodynamic and mechanistic studies. *Mater Chem Phys.* 2020;245:122737. doi: 10.1016/j.matchemphys.2020.122737
14. Tian F, Wu W, Jiang Z, *et al*. The study of thiophene adsorption onto La(III)-exchanged zeolite NaY by FT-IR spectroscopy. *J Colloid Interface Sci.* 2006;301:395-401. doi: 10.1016/j.jcis.2006.04.042
15. Kim JH, Ma X, Zhou A, Song C. Ultra-deep desulfurization and denitrogenation of diesel fuel by selective adsorption over three different adsorbents: A study on adsorptive selectivity and mechanism. *Catal Today.* 2006;111:74-83. doi: 10.1016/j.cattod.2005.11.012
16. Tang T, Zhang L, Fu W, *et al*. Design and synthesis of metal sulfide catalysts supported on zeolite nanofiber bundles with unprecedented hydrodesulfurization activities. *J Am Chem Soc.* 2013;135:11437-11440. doi: 10.1021/ja406393h
17. Lin L, Zhang Y, Zhang H, Lu F. Adsorption and solvent desorption behavior of ion-exchanged modified Y zeolites for sulfur removal and for fuel cell applications. *J Colloid Interface Sci*. 2011;360:753-759. doi: 10.1016/j.jcis.2011.06.040
18. Shi Y, Yang X, Tian F, Jia C, Chen Y. Effects of toluene on thiophene adsorption over NaY and Ce(IV)Y zeolites.

J Nat Gas Chem. 2012;21:421-425.
doi: 10.1016/S1003-9953(11)60394-9

19. Tian F, Shen Q, Fu Z, Wu Y, Jia C. Enhanced adsorption desulfurization performance over hierarchically structured zeolite Y. *Fuel Process Technol.* 2014;128:176-182.
doi: 10.1016/j.fuproc.2014.05.019
20. Lee KX, Valla JA. Investigation of metal-exchanged mesoporous Y zeolites for the adsorptive desulfurization of liquid fuels. *Appl Catal B.* 2017;201:359-369.
doi: 10.1016/j.apcatb.2016.07.028
21. Kalita P, Gupta NM, Kumar R. Synergistic role of acid sites in the Ce-enhanced activity of mesoporous Ce-Al-MCM-41 catalysts in alkylation reactions: FTIR and TPD-ammonia studies. *J Catal.* 2007;245:338-347.
doi: 10.1016/j.jcat.2006.11.004
22. Meng X, Qiu G, Wang G, Cai Q, Wang Y. Durable and regenerable mesoporous adsorbent for deep desulfurization of model jet fuel. *Fuel Process Technol.* 2013;111:78-85.
doi: 10.1016/j.fuproc.2013.03.009.
23. Shen Y, Li P, Xu X, Liu H. Selective adsorption for removing sulfur: A potential ultra-deep desulfurization approach of jet fuels. *RSC Adv.* 2012;2:1700-1711.
doi: 10.1039/C1RA00831A
24. Danmaliki GI, Saleh TA. Influence of conversion parameters of waste tires to activated carbon on adsorption of dibenzothiophene from model fuels. *J Clean Prod.* 2016;117:50-55.
doi: 10.1016/j.jclepro.2016.01.034
25. Vecchi PA, Ellern A, Angelici RJ. Synthetic, structural, and kinetic studies of $[CpRu(CO)_2(\mu_2\text{-}\ \eta^1(S):\mu^6\text{-DBT})\ RuCp^*][PF_6]_2$: A dibenzothiophene bridge between two ruthenium fragments. *Organometallics.* 2005;24:3725-3730.
doi: 10.1021/om050312s
26. Stoffregen SA, Vecchi PA, Ellern A, Angelici RJ. A new approach to the stabilization of dibenzothiophene (DBT) coordination to metals: Studies of $(\eta^5\text{-}C_5H_4CH_2Ph)Ru(CO)_2(\eta^1(S)\text{-DBT})^+$. *Inorg Chim Acta.* 2007;360:1711-1716.
doi: 10.1016/j.ica.2006.11.022
27. Song H, Cui X, Song H, Gao H, Li F. Characteristic and adsorption desulfurization performance of Ag-Ce bimetal ion-exchanged Y zeolite. *Ind Eng Chem Res.* 2014;53:14552-14557.
doi: 10.1021/ie503774e
28. Duan L, Gao X, Meng X, *et al*. Adsorption, co-adsorption, and reactions of sulfur compounds, aromatics, olefins over Ce-exchanged Y zeolite. *J Phys Chem C.* 2012;116:25748-25756.
doi: 10.1021/jp308013m
29. Xue M, Chitrakar R, Sakane K, *et al*. Preparation of cerium-loaded Y-zeolites for removal of organic sulfur compounds from hydrodesulfurizated gasoline and diesel oil. *J Colloid Interface Sci.* 2006;298:535-542.
doi: 10.1016/j.jcis.2006.04.028
30. Xing ZM, Gao YX, Shi LY, Liu XQ, Jiang Y, Sun LB. Fabrication of gold nanoparticles in confined spaces using solid-phase reduction: Significant enhancement of dispersion degree and catalytic activity. *Chem Eng Sci.* 2017;158:216-226.
doi: 10.1016/j.ces.2016.10.044
31. Wang W, Guo S, Lee K, *et al*. Hydrous ruthenium oxide nanoparticles anchored to graphene and carbon nanotube hybrid foam for supercapacitors. *Sci Rep.* 2014;4:4452-4460.
doi: 10.1038/srep04452
32. Hwang JY, El-Kady MF, Wang Y, *et al*. Direct preparation and processing of graphene/RuO_2 nanocomposite electrodes for high-performance capacitive energy storage. *Nano Energy.* 2015;18:57-70.
doi: 10.1016/j.nanoen.2015.06.011
33. Qadir K, Kim SM, Seo H, *et al*. Deactivation of Ru catalysts under catalytic CO oxidation by formation of bulk Ru oxide probed with ambient pressure XPS. *J Phys Chem C.* 2013;117:13108-13113.
doi: 10.1021/jp404548n
34. Lee JD. *A New Concise Inorganic Chemistry*. 3rd ed. Japanese: Van Nostrand Reinhold; 1977. p. 323.
35. Zhang Z, Ding L, Gu J, *et al*. 3D charged grid induces a high performance catalyst: Ruthenium clusters enclosed in X-zeolite for hydrogenation of phenol to cyclohexanone. *Catal Sci Technol.* 2017;7:5953-5963.
doi: 10.1039/C7CY01424G
36. Darwiche A, Bodenes L, Madec L, Monconduit L, Martinez H. Impact of the salts and solvents on the SEI formation in Sb/Na batteries: An XPS analysis. *Electrochim Acta.* 2016;207:284-292.
doi: 10.1016/j.electacta.2016.04.140
37. Thunyaratchatanon C, Luengnaruemitchai A, Chaisuwan T, Chollacoop N, Chen SY, Yoshimura Y. Synthesis and characterization of Zr incorporation into highly ordered mesostructured SBA-15 material and its performance for CO_2 adsorption. *Microporous Mesoporous Mater.* 2017;253:18-28.
doi: 10.1016/j.micromeso.2017.05.012
38. Xu L, Yan P, Li H, *et al*. Metallic Bi self-doping BiOCl composites: Synthesis and enhanced photoelectrochemical performance. *Mater Lett.* 2017;196:225-229.
doi: 10.1016/j.matlet.2017.02.025
39. Zheng HY, Wang JZ, Li Z, Yan LF, Wen JZ. Characterization and assessment of an enhanced CuY catalyst for oxidative carbonylation of methanol prepared by consecutive liquid-phase ion exchange and incipient wetness impregnation. *Fuel Process Technol.* 2016;152:367-374.
doi: 10.1016/j.fuproc.2016.01.023
40. Tang Q, Wang Y, Zhang Q, Wan H. Preparation of metallic cobalt inside NaY zeolite with high catalytic

activity in Fischer-Tropsch synthesis. *Catal Commun.* 2003;4:253-258.
doi: 10.1016/S1566-7367(03)00024-4

41. Cao Y, Zhuang TT, Yang J, Liu HD, Huang W, Zhu H. Promoting zeolite NaY as efficient nitrosamines trap by cobalt oxide modification. *J Phys Chem C.* 2007;111:538-548.
doi: 10.1021/jp066034u
42. Ge X, Shi L, Wang X. Dechlorination of reformate via chemical adsorption reactions by Ce-Y zeolite. *Ind Eng Chem Res.* 2014;53:6351-6357.
doi: 10.1021/ie404071z
43. Ahmed MHM, Muraza O, Jamil AK, Shafei EN, Yamani ZH, Choi K. Steam catalytic cracking of n-dodecane over Ni and Ni/Co bimetallic catalyst supported on hierarchical BEA zeolite. *Energy Fuels.* 2017;31:5482-5490.
doi: 10.1021/acs.energyfuels.7b00413
44. Zeng YJ, Yu HJ, Shi L. Surface acidity and catalytic activity of Y-zeolite catalysts. *J East China Univ Sci Technol Nat Sci Ed*. 2008;34(5):635-640.
45. Wang WY, Pan MX, Qin YC, Wang LT, Song LJ. Effects of surface acidity on the adsorption desulfurization of Cu(I) Y zeolites. *Acta Phys-Chim Sin.* 2011;27(5):1176-1180.
doi: 10.3866/PKU.WHXB20110442
46. Skarlis SA, Berthout D, Nicolle A, Dujardin C, Granger P. Multisite modeling of NH_3 adsorption and desorption over Fe-ZSM5. *J Phys Chem C.* 2012;116:8437-8448.
doi: 10.1021/jp302324q
47. Aslam S, Subhan F, Yan Z, *et al*. Unusual nickel dispersion in confined spaces of mesoporous silica by one-pot strategy for deep desulfurization of sulfur compounds and FCC gasoline. *Chem Eng J.* 2017;321:48-57.
doi: 10.1016/j.cej.2017.03.043
48. Bartholomew CH. Mechanisms of catalyst deactivation. *Appl Catal A Gen.* 2001;212:17-60.
doi: 10.1016/S0926-860X(00)00843-5
49. Song H, Jiang BL, Song HL, Jin ZS, Sun XL. Preparation of AgY zeolite and study on its adsorption equilibrium and kinetics. *Res Chem Intermed.* 2015;41:3837-3854.
doi: 10.1007/s11164-014-1844-z
50. Li J, Gyoten H, Sonoda A, Feng Q, Xue M. Removal of trace arsenic to below drinking water standards using a Mn-Fe binary oxide. *RSC Adv.* 2017;7:1490-1497.
doi: 10.1039/C6RA24862D
51. Xiong J, Yang L, Chao Y, *et al*. Boron nitride mesoporous nanowires with doped oxygen atoms for the remarkable adsorption desulfurization performance from fuels. *ACS Sustain Chem Eng.* 2016;4:4457-4464.
doi: 10.1021/acssuschemeng.6b00914